

Computer simulation of a liquid-crystal anchoring transition

F. Barmes

Centre Européen de Calcul Atomique et Moléculaire, 46 Allée d'Italie, 69007 Lyon, France

D. J. Cleaver

Materials Research Institute, Sheffield Hallam University, Sheffield, S1 1WB, United Kingdom

(Received 19 January 2004; published 2 June 2004)

We present a study of the effects of confinement on a system of hard Gaussian overlap particles interacting with planar substrates through the hard-needle-wall potential. Using geometrical arguments to calculate the molecular volume absorbed at the substrates, we show that both planar and homeotropic arrangements can be obtained using this model. Monte Carlo simulations are then used to perform a systematic study of the model's behavior as a function of the system density and the hard-needle-wall interaction parameter. As well as showing the homeotropic to planar anchoring transition, the anchoring phase diagrams computed from these simulations indicate regions of bistability. This bistable behavior is examined further through the explicit simulation of field-induced two-way switching between the two arrangements.

DOI: 10.1103/PhysRevE.69.061705

PACS number(s): 61.30.Cz, 64.70.Md, 68.08.-p

I. INTRODUCTION

Confinement of a liquid crystal has a symmetry breaking effect; this induces both positional layering and orientational coupling which is transmitted to the bulk alignment through a mechanism called anchoring [1]. While the former effect is a universal consequence of confinement [2,3], the latter is specific to mesogenic systems. For these, three main arrangements for the particles close to the surface can be observed, namely homeotropic, planar, and tilted. A range of azimuthal anchoring states are also possible. Upon change of experimental conditions, modification of the surface arrangement can be observed to lead to a change in the bulk alignment; such an event is called an anchoring transition [1].

Experimental studies of confined liquid crystals have reported that anchoring transitions can be achieved by various means such as change in temperature [4–6] or the conformation of the aligning agent [7,8]. Incident radiation can also induce anchoring transitions by selectively switching the conformations of substrate molecules and, thus, modifying the interfacial interactions [9]. Alternatively, the adsorption behavior of a liquid crystal at a solid substrate, either directly [10,11], or through the introduction of a second species [12], can lead to anchoring transitions if the density of adsorbed particles or the nature of the adsorption is changed. One last example is that in which a multistable anchored system, which preferentially adopts one of its possible conformations due to its treatment history [1,13], is switched into an alternative state by, e.g., an appropriate applied field.

Although a number of mechanisms underlying anchoring transitions have been raised (see [14] for a review) rather few theoretical analyses have been performed. Teixeira and Sluckin [15,16] used a Landau-de Gennes free energy functional to study the planar to homeotropic anchoring transition in liquid-crystal systems confined by different substrates. They found a rich anchoring behavior which helped in the identification of mechanisms responsible for the anchoring transitions, specifically, the compositions of binary mixtures of liquid crystals and the amount of adsorption at the surface.

Subsequently Teixeira *et al.* [17] used a Landau-de Gennes formalism to observe a temperature driven anchoring transition at the interface between a liquid crystal and smooth solid surface, thus confirming the experimental findings. The effect of nonuniform substrates (i.e., microtexture) has also been studied using a Landau-de Gennes formalism [18,19]. This work found temperature-driven phase-transitions between states with different tilt angles.

In the field of molecular simulations, the effects of confinement on liquid crystalline systems has been increasingly well studied, and all of the surface arrangements listed above have been obtained through appropriate choices of particle-surface interaction potential. Using various parameterizations of the Gay-Berne model [20] and taking the particle-wall contact distance to be that between a rod and a sphere, both tilted and planar anchoring states have been observed [21–24]. If, alternatively, the surface is represented using a monolayer of spheres, the particle-substrate interaction can be designed to induce either homeotropic or planar anchoring [25–27]. Using hard ellipsoids confined so that their centers of mass interacted sterically with smooth substrates, Allen [28] observed homeotropic surface arrangement. Subsequently van Roij *et al.* [29–31] investigated the behavior of hard spherocylinders at a hard smooth wall and observed surface-induced wetting and planar ordering. These studies also showed that the planar arrangement is the natural state of hard-rod nematic phase in contact with a flat surface. Chrzanowska *et al.* and Cleaver *et al.* [32,33] used the hard Gaussian overlap (HGO) model [34] (i.e., a hard version of the Gay-Berne model) to investigate confined symmetric and hybrid anchored films using the hard-needle-wall (HNW) potential as a surface model. Here, simulations of symmetrically anchored systems showed that, with appropriate tuning, this surface model can induce either homeotropic or planar anchoring, a finding which we expand upon in the current paper.

Liquid-crystal adsorption has also been studied using simulations of all-atom models, investigating, for example, the behavior of 8CB on various substrates [35–37]. These

studies gave results which were largely consistent with scanning tunneling microscopy investigations with respect to the structure of the observed planar arrangements. A more systematic series of simulation was performed subsequently by Binger and Hanna [38–40] who simulated the adsorption of several liquid crystals (e.g., 5CB, 8CB, MBF). Systems ranging from single molecules up to two monolayers anchored on different polymeric substrates (e.g., PE, PVE, Nylon 6) were investigated. From this, the authors found that, for most substrates, the liquid crystals adopted planar arrangements with some specific conformations being favored; conversely, Dorrer and Taylor [41,42] reported preferential homeotropic anchoring from their simulations of 5CB on amorphous PE.

Comparatively, the literature on computer simulations of anchoring transitions is extremely scarce. Using HGO and HNW potentials for, respectively, intermolecular and surface interactions, Cleaver and Teixeira [33] have found a density-driven homeotropic to planar anchoring transition at one wall of a model cell with hybridly set boundaries. Also, more recently, Lange and Schmid [43–45] have observed an anchoring transition in a system of ellipsoidal Gay-Berne particles confined by grafted polymer chains. Here, the transition between tilted and homeotropic arrangements was induced by changes in the grafting density.

In this paper, we use Monte Carlo simulations to study the effects of confinement on a system of model mesogenic particles and so gain a microscopic understanding of their anchoring transition. This paper is organized as follows: the models used for this study are described in Sec. II. The model's surface induced structural changes are studied in Sec. III through observation of typical profiles obtained from the simulations and the dependence of these profiles on the surface potential and the system density. From this, in Sec. IV, we obtain a comprehensive mapping of the model's anchoring behavior, including the identification and localization of its planar to homeotropic anchoring transition. This section also contains an explicit study of the anchoring bistability found to be associated with this transition. The conclusions drawn from this work and a description of future studies are given in Sec. V.

II. THE MODEL

Here, surface induced structural changes are studied using Monte Carlo simulations of rod-shaped particles that interact with one another through the hard Gaussian overlap (HGO) potential [46] and with the confining substrates via the hard-needle-wall (HNW) potential. The latter was used since it provides a simple and intuitive steric interaction which can be tuned so as to induce either homeotropic or planar anchoring arrangements [32,33]. It also lends itself to the straightforward development of geometry-based predictions with which to compare simulation results. Despite this simplicity, however, the HNW potential is able to exhibit both anchoring transitions and bistability.

The HGO model is a steric model in which the contact distance is the shape parameter determined by Berne and Pechukas [34] when they considered the overlap of two ellipsoidal Gaussian. Thus the interaction potential ν^{HGO} be-

tween two particles i and j with respective orientations $\hat{\mathbf{u}}_i$ and $\hat{\mathbf{u}}_j$ and intermolecular vector $\mathbf{r}_{ij}=r_{ij}\hat{\mathbf{r}}_{ij}$ is defined as

$$\nu^{\text{HGO}} = \begin{cases} 0 & \text{if } r_{ij} \geq \sigma(\hat{\mathbf{u}}_i, \hat{\mathbf{u}}_j, \hat{\mathbf{r}}_{ij}) \\ \infty & \text{if } r_{ij} < \sigma(\hat{\mathbf{u}}_i, \hat{\mathbf{u}}_j, \hat{\mathbf{r}}_{ij}) \end{cases} \quad (1)$$

where $\sigma(\hat{\mathbf{u}}_i, \hat{\mathbf{u}}_j, \hat{\mathbf{r}}_{ij})$ is the contact distance

$$\sigma(\hat{\mathbf{u}}_i, \hat{\mathbf{u}}_j, \hat{\mathbf{r}}_{ij}) = \sigma_0 \left\{ 1 - \frac{1}{2} \chi \left[\frac{(\hat{\mathbf{r}}_{ij} \cdot \hat{\mathbf{u}}_i + \hat{\mathbf{r}}_{ij} \cdot \hat{\mathbf{u}}_j)^2}{1 + \chi(\hat{\mathbf{u}}_i \cdot \hat{\mathbf{u}}_j)} + \frac{(\hat{\mathbf{r}}_{ij} \cdot \hat{\mathbf{u}}_i - \hat{\mathbf{r}}_{ij} \cdot \hat{\mathbf{u}}_j)^2}{1 - \chi(\hat{\mathbf{u}}_i \cdot \hat{\mathbf{u}}_j)} \right] \right\}^{-1/2}. \quad (2)$$

Here σ_0 , the particle width, sets the unit of distance for this model and the shape anisotropy parameter $\chi=(k^2-1)/(k^2+1)$ where $k=\sigma_l/\sigma_0$ is the particle length-to-breadth ratio.

The HGO model is the hard-particle equivalent of the much-studied Gay-Berne model [20]. The phase behavior of the HGO model is density driven and fairly simple, comprising only two noncrystalline phases; isotropic and (for $k \geq 3$) nematic fluids at, respectively, low and high number densities ρ^* . The isotropic-nematic phase-coexistence densities have been located for various particle elongations in a series of previous Monte Carlo simulation studies [47–49]; for the most commonly used elongation of $k=3$, the transition occurs for $\rho^* \approx 0.30$ with a slight system size dependence. Our own simulations of 3d bulk systems of $N=1000$ particles [50,51] have found isotropic (nematic) coexistence densities of $\rho_l^*=0.299$ ($\rho_N^*=0.309$), in agreement with these previous studies. Although the HGO model was originally derived using geometrical considerations, an HGO particle cannot be represented by a fixed solid object. Rather, it is a mathematical abstraction of the interaction surface between two non-spherical particles [46]. For moderate elongations, however, the properties of HGO particles are similar to those of an equivalent hard ellipsoid of revolution [46]. Simulation studies [49] have borne this out, showing that the equation of state of the HGO fluid is qualitatively equivalent to, but consistently displaced from, that of the hard ellipsoid fluid.

In this paper, we sidestep the issue of how an undefined HGO particle should interact with a planar substrate (this is addressed elsewhere [50,52]) since here the HNW potential has been used for the particle-wall interaction. In this, the particle surfaces do not interact directly with the substrates; rather the interaction is mediated by axial needles placed at the centers of the HGO particles (Fig. 1). The interaction potential between particle i and a planar substrate located at $z=z_0$ is, thus, given by [33]

$$\nu^{\text{HNW}} = \begin{cases} 0 & \text{if } |z_i - z_0| \geq \sigma_w(\hat{\mathbf{u}}_i) \\ \infty & \text{if } |z_i - z_0| < \sigma_w(\hat{\mathbf{u}}_i) \end{cases} \quad (3)$$

where

$$\sigma_w(\hat{\mathbf{u}}_i) = \frac{1}{2} \sigma_0 k_S \cos(\theta_i). \quad (4)$$

Here, k_S is the dimensionless needle length and $\theta_i = \arccos(u_{i,z})$ is the angle between the substrate normal and

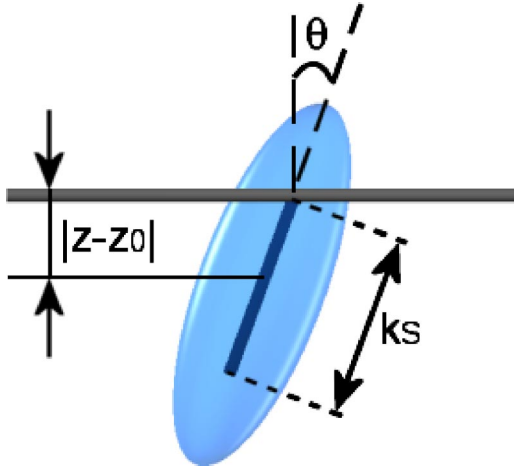


FIG. 1. (Color online) Schematic representation of the geometry used for the hard-needle-wall particle-surface interaction.

the particle's orientation vector, which also corresponds to the zenithal Euler angle (Fig. 1).

The surface behavior of the HNW model has previously been studied in slab-geometry by Cleaver and Teixeira [33] and Chrzanowska *et al.* [32]. Also the model simulated by Allen [28], in which the particle centers of mass were taken to interact sterically with the substrate, corresponds to the HNW potential with $k_S=0$. For small k_S , the homeotropic arrangement has been shown to be stable, whereas planar anchoring is favored for long k_S . Insight can be gained into this transition by noting that, in the limit of perfect orientational and positional order, the Helmholtz free energy of this system is minimized by the arrangement that maximizes the particle volume absorbed into the substrates. For all k and $k_S \neq 0$, the absorbed volume of a single particle is clearly maximal for $\theta = \pi/2$, suggesting that the planar arrangement should always be stable (for the case $k_S=0$, planar and homeotropic alignments both allow the absorption of half the particle volume). For many body systems, however, it is also necessary to consider the relative packing efficiencies of the two arrangements.

To this end, we now consider the behavior of a system of HGO particles in a fixed volume, one face of which is bounded by an HNW potential substrate. The aim is to calculate the homeotropic to planar transition needle length for this system. For simplicity, each particle close to the surface is approximated to be an ellipsoid of revolution [46] with elongation $k = \sigma_\ell / \sigma_0$ and semiaxis lengths $a = b = \sigma_0/2$ and $c = \sigma_\ell/2$. The homeotropic to planar transition needle length can then be determined by equating the ratio of the volume absorbed per unit area of the substrate for the two key arrangements. In the limit of perfect order, symmetry details of the packing can be ignored in this calculation since they must be the same for both anchoring alignments; the two arrangements will map onto each other via suitable affine transformations.

In the case of planar alignment, the adsorbed volume and occupied area are independent of k_S and their ratio is simply $\sigma_0/3$. The homeotropic case is rather more involved, since although the projected area of each particle onto the surface

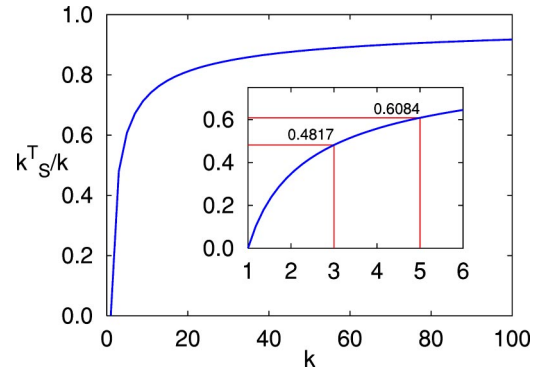


FIG. 2. (Color online) Predicted variation of k_S^T/k with k in the high packing limit.

is constant, the particle-substrate distances are now dependent on k_S . In the ellipsoidal-particle approximation, the escaped volume for such a particle can be shown to be

$$V_e = \frac{\pi\sigma_0^2}{4} \left[\frac{k_S}{2} \left(\frac{k_S^2}{3\sigma_\ell^2} - 1 \right) + \frac{\sigma_\ell}{3} \right]. \quad (5)$$

Using this result, the needle length corresponding to the planar-homeotropic transition is then given by the root k_S^T of

$$\frac{1}{6k^2\sigma_0^2}k_S^3 - \frac{1}{2}k_S + \frac{\sigma_0}{3}(k-1) = 0 \quad (6)$$

satisfying $k_S^T \in]0 : k]$. The result is k -dependent; the variation of the transition k_S^T/k as a function of k is shown in Fig. 2. For the two particle elongations used in the simulation part of this study, that is $k=3$ and 5 , the predicted transition needle lengths are $k_S^T/k=0.48$ and 0.61 , respectively.

III. SIMULATION OF SYMMETRICALLY ANCHORED SYSTEMS

Here, we present the results from a comprehensive Monte Carlo simulation study of HGO systems confined between symmetrical HNW substrates. All of the simulations were performed in the canonical ensemble on systems of $N = 1000$ particles. Particle elongations $k=3$ and 5 were both studied, but for reasons of space we restrict ourselves, in most cases, to showing results for the $k=3$ systems only. The substrates were separated by a distance $L_z = 4k\sigma_0$ and were located at $z = \pm L_z/2$, the system being periodic in the x and y directions. The simulation box lengths in these other directions were determined by the imposed number density, ρ^* , through the relationship $L_x = L_y = \sqrt{N/(\rho^* L_z)}$. In each simulation, the same substrate potential (i.e., k_S value) was applied at each wall, so that all of the results presented relate to symmetric anchoring situations. That restriction apart, a systematic study of the k_S and ρ^* dependence of these systems has been undertaken; Figs. 3(a) and 3(b) show the state points at which simulations were performed as well as the directions of the various simulation series. The simulation series directions are given since, at some state points, the anchoring adopted by the system was found to be dependent on that of the initial configuration employed. Typical run

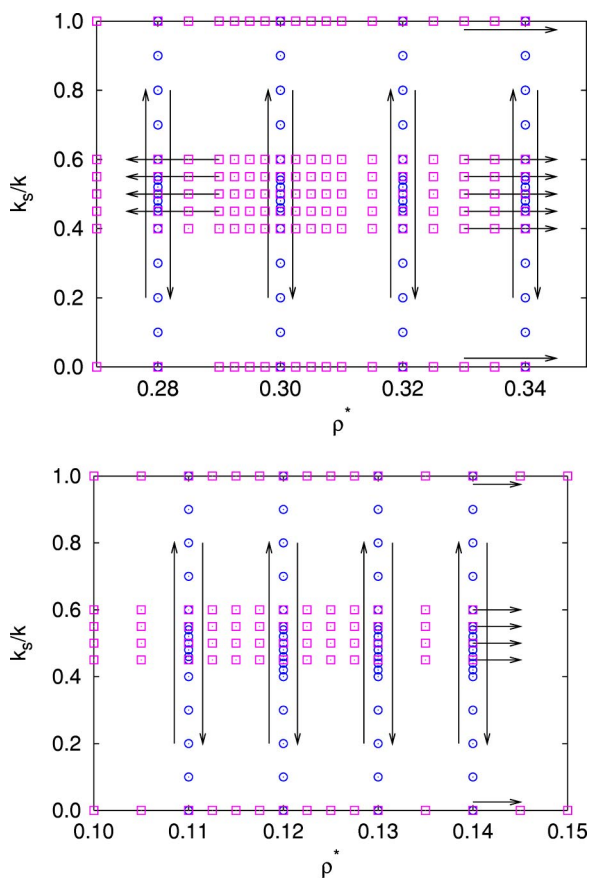


FIG. 3. (Color online) Representation of the state points considered in the simulations presented in this paper. The arrows represent the direction in which the simulations series were performed.

lengths at each state point were 0.5×10^6 Monte Carlo (MC) sweeps (where one sweep represents one attempted move per particle) of equilibration followed by a production run of 0.5×10^6 sweeps.

The relatively modest system size of $N=1000$ has been used here in order to enable a comprehensive mapping of the relevant phase space to be achieved. From De Miguel’s study of system size effects in 3D bulk systems of Gay-Berne particles [53], it is apparent that any N -dependence of bulk behavior should be negligible for $N = \mathcal{O}(10^3)$. This conclusion does not transfer automatically to confined systems, however, since the surface extrapolation lengths can become comparable with the substrate-substrate separation [54]. For the systems studied here, in which the surface conditions were symmetrical, we have found that doubling the slab thickness (i.e., running with $N=2000$ particles) does not have a significant effect on the anchoring behavior observed. However, in equivalent simulations of hybrid anchored systems, in which the two surface extrapolation length regions can promote competing effects, we have found that the slab thickness becomes a significant simulation parameter [50,55].

We present the simulation results by first describing the typical behaviors exhibited by these systems. We then go on to assess the global phase and structural dependence on the imposed number density, ρ^* , and internal needle length $k_S\sigma_0$

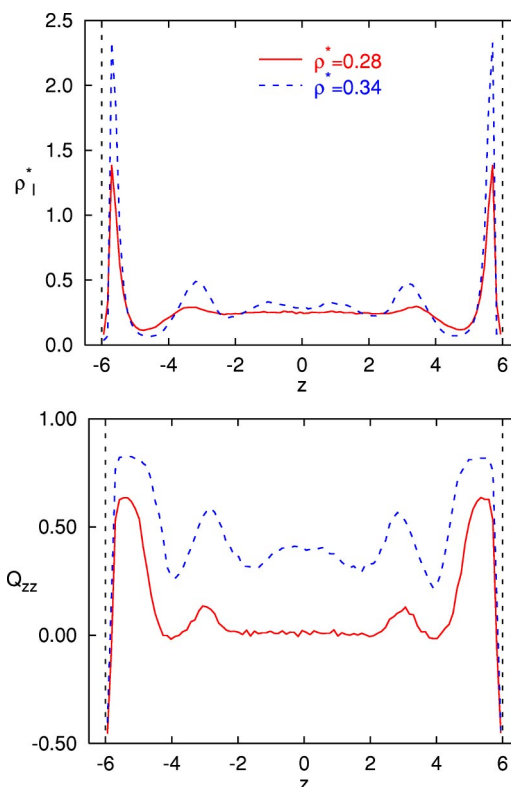


FIG. 4. (Color online) Typical profiles corresponding to homeotropic anchoring for $k=3$ and $k_S/k=0.20$ as obtained from simulation series at constant density and decreasing needle length.

before, in the next section, going on to construct anchoring maps and make an explicit examination of the bistability displayed by one system.

Initial analysis of the surface-induced structural changes has been performed using profiles of the number density, $\rho_\ell^*(z)$, and the orientational order measured with respect to the substrate normal

$$Q_{zz}(z) = \frac{1}{N(z)} \sum_{i=1}^{N(z)} \left(\frac{3}{2} u_{i,z}^2 - \frac{1}{2} \right) \quad (7)$$

where $N(z)$ is the instantaneous occupancy of the layer. Typical profiles for bulk isotropic and nematic densities are shown for homeotropic ($k_S < k_S^T$), planar ($k_S > k_S^T$), and competing ($k_S \sim k_S^T$) anchoring arrangements in Figs. 4–6.

Homeotropic alignment was observed when the HNW potential was characterized by a short needle length. Thus Fig. 4 shows that with $k=3$ and $k_S/k=0.2$, $\rho_\ell^*(z)$ was dominated by surface-layer peaks at $|z-z_0| \sim k_S\sigma_0/2$. Small secondary features, displaced by $k\sigma_0$ from the surface peaks, are apparent at the nematic density, consistent with an arrangement which involved smectic-like layers templated by the substrates. The corresponding $Q_{zz}(z)$ profiles confirm this homeotropic arrangement, showing positive values in regions of high $\rho_\ell^*(z)$, that is the interfacial regions for both densities and the bulk region at the nematic density. The oscillations in $Q_{zz}(z)$ correlate closely with those in $\rho_\ell^*(z)$ due to both the intrinsic coupling between density and order parameter and

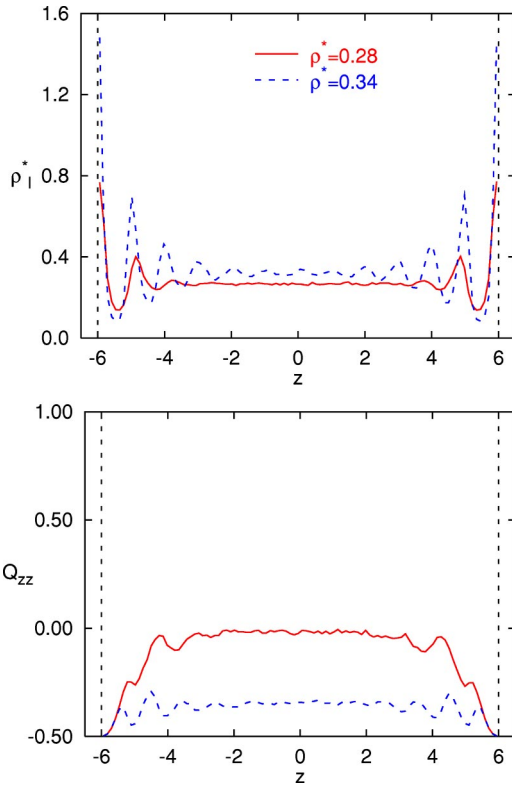


FIG. 5. (Color online) Typical profiles corresponding to a planar arrangement with $k=3$ and $k_S/k=0.80$ as obtained from simulation series at constant density and decreasing needle length.

the homeotropic director-pinning imposed by the smectic-like layers. Additionally, regardless of the number density, $Q_{zz}(z)$ displays negative values very close to the substrates ($|z-z_0| \leq k_S\sigma_0/2$); these features occur because the HNW potential dictates that any particles in these regions must be tilted away from the substrate normal. These regions with negative $Q_{zz}(z)$ values have very low number densities, however, and so are of little practical significance.

For planar alignment situations, such as that observed for $k=3$ and $k_S/k=0.8$, the density and order profiles adopted the forms shown in Fig. 5. Here, because the surface layers were dominated by planar-aligned particles, the main peaks in ρ_ℓ^* are located at $|z-z_0| \sim 0$. The peak-peak separations in the nematic-density $\rho_\ell^*(z)$ are also much smaller than those seen in the homeotropic case (approximately σ_0 rather than $k_S\sigma_0$), since here the particles in neighboring strata had a side-by-side arrangement (i.e., they were *not* in smectic-like layers). Again, the features in the $Q_{zz}(z)$ profiles correspond closely with those in $\rho_\ell^*(z)$, but this time the maxima in ρ_ℓ^* relate to minima in $Q_{zz}(z)$ since planar order results in negative values of $Q_{zz}(z)$.

For some k_S values intermediate between the two cases just presented, situations were found in which the relative stability of the planar and homeotropic arrangements was unclear. Generally this situation arose in nematic systems for which $k_S \sim k_S^T$. Typical profiles corresponding to this competing anchoring situation are shown in Fig. 6 for $k=3$ and $k_S/k=0.48$, i.e., a needle length very close to the k_S^T value given by Eq. (6). Here, at high number densities, two sets of

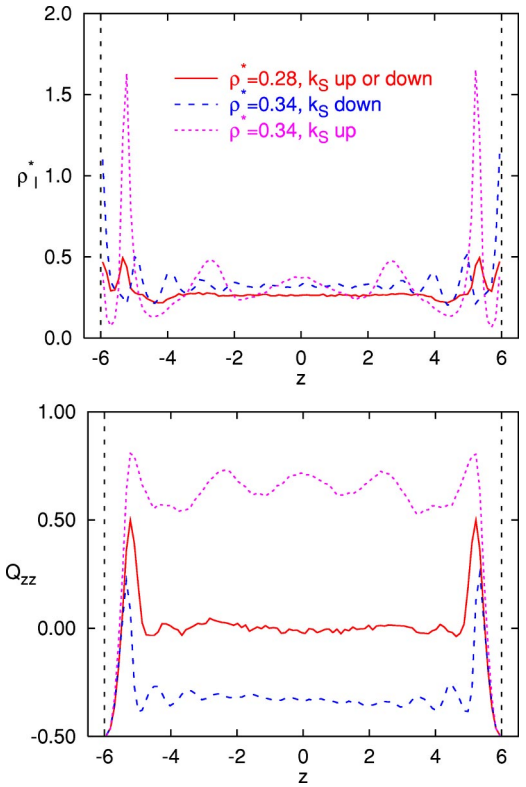


FIG. 6. (Color online) Typical profiles for $k=3$ and $k_S/k=0.48$. The term k_S up or down in the key of this figure refers to whether the profiles have been obtained from simulation with increasing (up) or decreasing (down) needle length.

profiles (corresponding to different surface arrangements) were obtained depending on the history of the simulation sequence. Since, in each case, these profiles were obtained from runs equilibrated over $\sim 10^6$ MC sweeps, bistability is suggested.

The $\rho^*=0.28$ profiles shown in Fig. 6 are noteworthy, since they contain features suggesting both planar and homeotropic influences. For example, the interfacial regions are characterized by two peaks, of comparable height, corresponding to substrate distances of $|z-z_0|=0$ and $k_S\sigma_0/2$, respectively. This double peaked behavior can be observed in both the $\rho_\ell^*(z)$ and the $Q_{zz}(z)$ profiles; in the latter it is manifested by the positive and negative regions corresponding to the peaks in the local density.

The two sets of $\rho^*=0.34$ profiles shown in Fig. 6 are very different from one another, and indicate that the two surface arrangements shown at this density in Fig. 4 and 5 were both accessible for this k_S value. The planar state was obtained when, in a series of runs performed at fixed density, the k_S value was decremented between runs, whereas the homeotropic arrangement was formed in an equivalent sequence performed with increasing k_S values. An interesting sign change is apparent in the $Q_{zz}(z)$ profile for the planar $\rho^*=0.34$ state. Here, while the surface and bulk alignment were both unquestionably planar, positive Q_{zz} values were obtained for $|z-z_0| \simeq k_S\sigma_0/2$, indicating, rather surprisingly, localized regions with net homeotropic alignment. This behavior was also seen for systems whose k_S values were sufficiently large

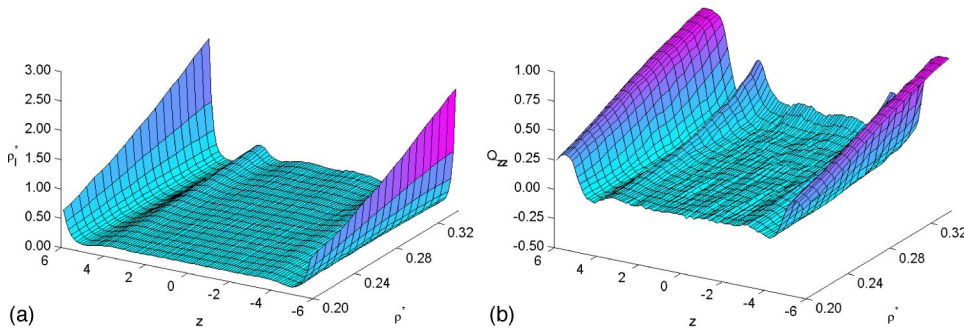


FIG. 7. (Color online) Surfaces showing the influence of ρ^* on systems with $k=3$ and $k_S/k=0.0$ (strongly homeotropic anchoring). These data are extracted from simulation series with decreasing needle length.

for the planar aligned state to be unambiguously stable, and so is unrelated to the possible bistability noted above. Instead, we attribute this behavior to the effect of particle-particle interactions on the θ -dependence of the orientational distribution function at these z values. For example, we note that at these wall separations, a particle orientation corresponding to modest tilt away from the substrate normal is disfavored since the resulting gap opened up between the tilted particle and the substrate would be too small to be occupied by a second particle. Consequently, the effect of the interactions between the tilted particle and its neighbors would be either to close the gap (by shifting the particle towards the substrate or rotating its orientation closer to the substrate normal) or to make the gap big enough for a second particle to enter (by making the particle more planar). This relative instability of moderate tilt angles at these wall separations is, we consider, the primary cause of the positive Q_{zz} values noted above.

Having described the behaviors exhibited by these systems, we now consider their ρ^* - and k_S -dependences by presenting the results from a more comprehensive investigation. In order to study the influence of density, several series of simulations were carried out at constant k_S values and increasing and decreasing densities. From these, $\rho_\ell^*(z, \rho^*)$ and $Q_{zz}(z, \rho^*)$ surfaces were computed for a range of k_S values. Results for the cases $k_S/k=0.0$ and $k_S/k=1.0$ are shown in Figs. 7 and 8 for $k=3$. Because little hysteresis was found between the series performed with increasing and decreasing densities, only the data obtained from the latter series are shown.

The surfaces shown in Figs. 7 and 8 largely confirm the observations made previously. At low densities, the surface induced effects are limited to the surface regions. With increase in density, however, the number of peaks in $\rho_\ell^*(z)$ increases steadily with ρ^* due to enhanced layering of the particles. Surface-induced order can be seen to extend further

into the cell with increase in ρ^* , largely reflecting the features apparent in the $\rho_\ell^*(z)$ surfaces. In the case of extreme homeotropic anchoring ($k_S/k=0.0$), regardless of the density, the central region of the cell failed to adopt nematic order. This was because, for this reduced needle length, the particle volume absorbed by the substrates reduced the bulk region density sufficiently to shift the $I-N$ transition to ρ^* values outside the range considered here. This does not, however, question the existence of uniform alignment in the case $k_S=0.0$. For the $k_S/k=1.0$ surface, orientational ordering of approximately the central 50% of the system can be seen to have taken place very uniformly. Relatively long runs were needed to establish this behavior since, at densities with isotropic bulk regions, there was little azimuthal coupling between the two ordered surface regions.

In order to generate equivalent information on the influence of k_S/k on the cell's behavior, further series of simulations were performed at constant densities with both increasing and decreasing needle lengths. Results from the series with decreasing k_S/k , $k=3$, and densities $\rho^*=0.28$ and 0.34 are shown as surfaces of $\rho_\ell^*(z, k_S/k)$ and $Q_{zz}(z, k_S/k)$ in Figs. 9 and 10, respectively. The differences found between the series performed with increasing and decreasing k_S/k are discussed in the next section.

From Figs. 9 and 10, the features discussed previously for strong homeotropic and planar anchoring arrangements can be seen at low and high values of k_S/k , respectively. A clear distinction can be made between the two anchoring regions from each of these surfaces, and a homeotropic to planar anchoring transition is again evident. As the transition region is approached from either high or low k_S , the peak heights of the ρ_ℓ^* surface decrease quite rapidly. At low density, remnants of these peaks remain at the transition, leading to bimodal surface layers which have features corresponding to both anchoring states. At nematic densities, in contrast, the crossover from one structure to the other is quite sharp. For

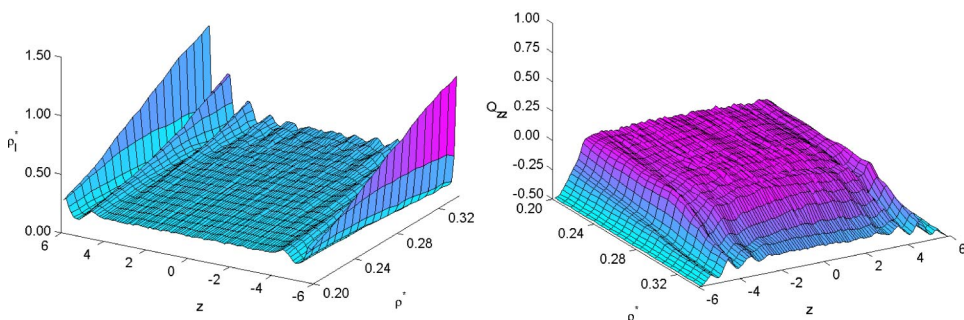


FIG. 8. (Color online) Surfaces showing the influence of ρ^* on systems with $k=3$ and $k_S/k=1.0$ (strongly planar anchoring). These data are extracted from simulation series with decreasing needle length.

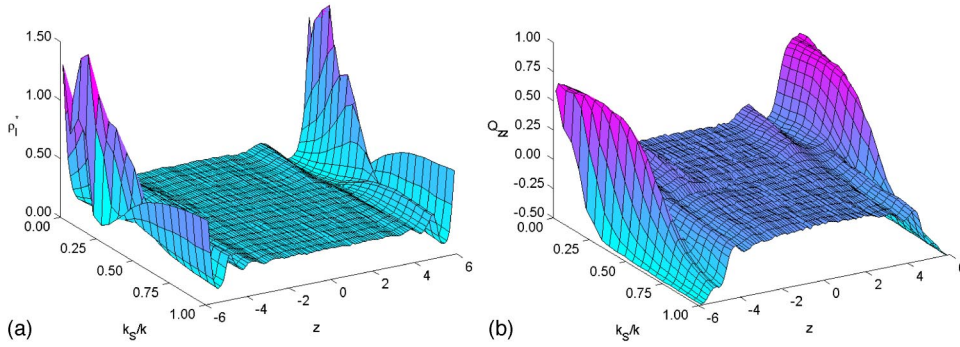


FIG. 9. (Color online) Surfaces showing the influence of k_S/k on systems with $k=3$ and $\rho^*=0.28$. These data are extracted from simulation series with decreasing needle length.

the $\rho_\ell^*(z, k_S/k)$ surfaces shown in Figs. 9 and 10, the z -values of the peaks on the two sides of the transition are clearly not coincident. The associated $Q_{zz}(z, k_S/k)$ surfaces give an obvious signature of the homeotropic to planar transition due to the sign change they exhibit. This change is relatively smooth in the surface regions, but is very sharp in the bulk region of the nematic density system. The gradient of this change was also found to increase with k ; the transition was much sharper for $k=5$ than for $k=3$.

IV. ANCHORING MAPS AND BISTABILITY

A phase-space mapping of the planar to homeotropic anchoring transition region needs to be expressed in terms of some quantitative indicator of the arrangement displayed by a given confined system. A useful measure for the characterization of the surface arrangement would be a scalar capable of indicating both the type and strength of the anchoring for a given $(\rho^*, k_S/k)$ state point. To this end, we introduce \bar{Q}_{zz} , a density-profile-weighted average of $Q_{zz}(z)$ taken over a given region of interest. We define \bar{Q}_{zz} as

$$\bar{Q}_{zz} = \frac{\sum_{z_i} Q_{zz}^n(z_i) \rho_\ell^*(z_i)}{\sum_{z_i} \rho_\ell^*(z_i)} \quad (8)$$

where the z_i considered are restricted to a given region of interest (i.e., bulk or surface). Here $Q_{zz}^n(z) \in [-1 : 1]$ is a pragmatically rescaled version of Q_{zz} defined by

$$Q_{zz}^n = \begin{cases} Q_{zz} & \text{if } Q_{zz} \geq 0 \\ 2 \cdot Q_{zz} & \text{if } Q_{zz} < 0. \end{cases} \quad (9)$$

In order for \bar{Q}_{zz} to be an objective measure, a criterion is needed with which to set the range of z_i to be included in its evaluation for, say, a surface region. Clearly, this limiting z_i needs to be located at a point at which the surface has no direct influence on the molecules. An apparently attractive choice for this would therefore be the distance at which the particles can rotate freely without direct interaction with the surface, i.e., $|z_i - z_0| = k_S \sigma_0 / 2$. This approach is flawed, however, since in the limit of zero needle length, it implies $|z_i - z_0| \sim 0$ whereas the surface layers clearly have finite thicknesses for all needle lengths.

Instead, the following approach was adopted in defining this limit; the surface region width was made a function of the needle length and density by making the limiting z_i value dependent on features of the measured density profiles. Explicitly, where the anchoring was found to be planar (with the first local maximum of $\rho_\ell^*(z)$ at $|z_i - z_0| \sim 0$), the surface region was taken to extend from the substrate to the distance corresponding to the second maximum in $\rho_\ell^*(z)$. If, however, the anchoring was homeotropic [with the first local maximum of $\rho_\ell^*(z)$ at $|z_i - z_0| \sim k_S \sigma_0 / 2$], the surface region was taken to extend from the substrate to the first local minimum in $\rho_\ell^*(z)$. In those cases with ambiguous, double-peaked density profiles, the former scheme was adopted. In all cases, the bulk region was taken to be that part of the system not included in the surface regions.

In what follows, maps of \bar{Q}_{zz} plotted as a function of ρ^* and k_S/k are used to construct anchoring maps. Such diagrams have been determined for systems with elongations $k=3$ and $k=5$ using data from the series of simulations performed at constant densities and both increasing and decreasing

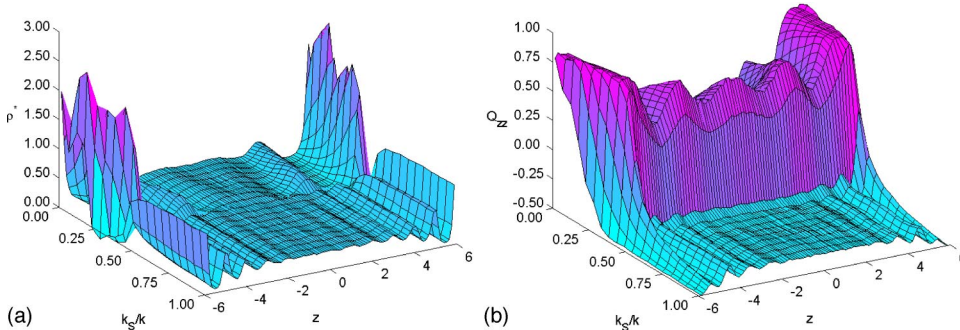


FIG. 10. (Color online) Surfaces showing the influence of k_S/k on systems with $k=3$ and $\rho^*=0.34$. These data are extracted from simulation series with decreasing needle length.

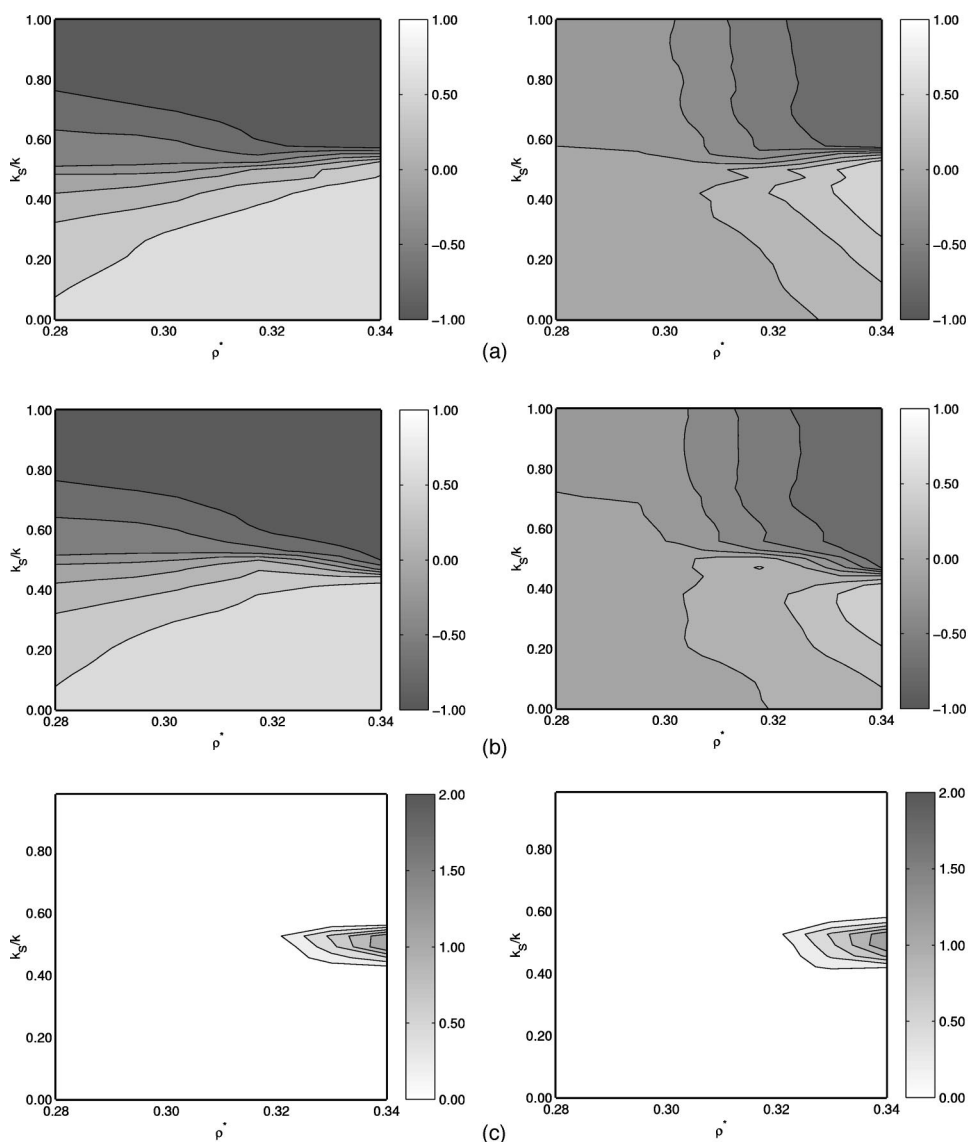


FIG. 11. Anchoring maps of \overline{Q}_{zz} for $k=3$ for the surface and bulk regions of the cell. Diagrams on the left-hand side are relative to the interfacial region and those on the right-hand side are relative to the bulk region. (a) Anchoring maps for series with increasing k_S/k . (b) Anchoring maps for series with decreasing k_S/k . (c) Bistability diagrams [i.e., difference between (a) and (b)].

ing needle lengths (recall Fig. 3). Results for both series in the surface (*Su*) and bulk (*Bu*) regions are shown in Fig. 11 and 12 for $k=3$ and $k=5$, respectively.

The results obtained for the two elongations are qualitatively similar. In the surface region diagrams, the anchoring transitions occur at k_S/k values close to those predicted in Sec. II, as can be observed from the lines of $\overline{Q}_{zz}^{Su}=0$. This agreement can be seen to improve with increase in density. Also the contour line spacing around k_S^T becomes tighter with increasing density, indicating a possible discontinuous transition between the planar and homeotropic anchoring states. In the bulk region diagrams, by comparison, little surface influence can be observed at low densities because the values of \overline{Q}_{zz}^{Bu} are limited by these systems' orientational isotropy. At number densities corresponding to bulk nematic order, however, the surface influence extends into the bulk region and sharp anchoring transitions become apparent at needle lengths similar to those suggested by the surface region anchoring diagrams. It is noteworthy that this effect is generally seen at global number densities significantly greater than the *I-N* transition densities of the equivalent bulk systems.

This indicates that the local densities found in the bulk regions were lower than the imposed ρ^* values due to the absorbing nature of the substrates.

The anchoring maps are asymmetric in that bulk planar ordering develops at lower densities than its homeotropic counterpart. This is due, in part, to the k_S -dependence of the volume absorption by the substrates, leading to the approximately bilinear dependence of ρ_{NI}^* on k_S seen in the \overline{Q}_{zz}^{Bu} anchoring maps. As noted previously, in the limit $k_S=0$, this absorption has proved sufficient to prevent the onset of bulk nematic for the range of ρ^* considered here. In addition to this bilinear k_S dependence, a further increase in ρ_{NI}^* can be observed at $k_S \approx k_S^T$. We attribute this anomalous behavior to the competing anchoring effects experienced by these systems. As was noted previously, the profiles obtained for such systems contain features associated with both of the anchoring arrangements. This, we suggest, leads to relatively disordered surface regions in these systems which, in turn, causes a delay in the onset of bulk-region nematic order.

Another interesting feature of Figs. 11 and 12 comes from the comparison of the diagrams for increasing and decreasing

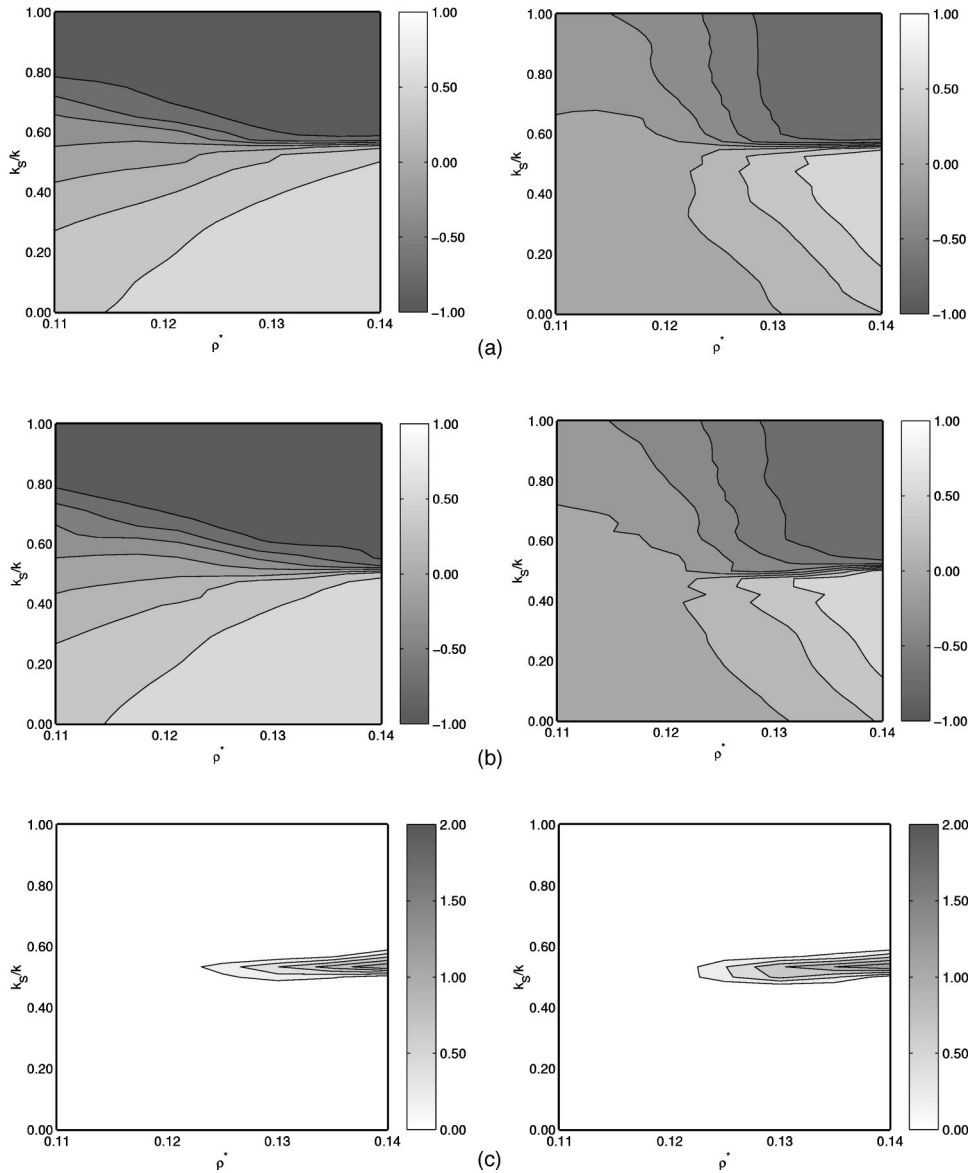


FIG. 12. Anchoring maps of $\overline{Q_{zz}}$ for $k=5$ for the surface and bulk regions of the cell. Diagrams on the left-hand side are relative to the interfacial region and those on the right-hand side are relative to the bulk region. (a) Series with increasing k_S/k . (b) Series with decreasing k_S/k . (c) Bistability phase diagram [i.e., difference between (a) and (b)].

needle lengths. At high densities, this confirms the earlier observation that, in conditions corresponding to competing anchoring, the structure adopted becomes dependent on system history. This suggests possible bistable behavior, on the “time scales” of our simulations at least, for state points close to the anchoring transition. The extent of this bistability has been evaluated by computation of the absolute value of the difference between the results obtained with series of increasing and decreasing needle lengths. These bistability maps, shown in Figs. 11(c) and 12(c), indicate distinct bistable regions at nematic densities for both $k=3$ and $k=5$.

In order to examine this behavior more explicitly, a final series of simulations has been performed in an attempt to switch the cell from planar to homeotropic and back again. For this, a previously equilibrated planar anchored system of $N=1000$ particles with $k=3$, $\rho^*=0.34$, and $k_S/k=0.5$ was used as the initial configuration. The switching was then performed through the series of simulations R_1 to R_5 listed in Table I, i.e., by applying and removing an electric field $\mathbf{E} = E\hat{z}$ and taking the dielectric anisotropy χ_e to be, alternately,

positive and negative. The effect of this was to align the particles parallel or perpendicular to \mathbf{E} for positive and negative values of χ_e , respectively. While this setup is admittedly somewhat unrealistic, it can be related to a putative experimental system in which the mesogen’s dielectric coupling varies according to the frequency of an applied ac field.

TABLE I. Parameterizations used to perform the switching between the planar and homeotropic states of the bistable system. Run lengths are given in Monte Carlo sweeps.

Run	$\hat{\mathbf{E}}$	E	χ_e	Run length
R_1	(0,0,0)	0.0	0.0	0.25×10^6
R_2	(0,0,1)	6.0	0.5	0.25×10^6
R_3	(0,0,0)	0.0	0.0	1.00×10^6
R_4	(0,0,1)	6.0	-0.5	0.25×10^6
R_5	(0,0,0)	0.0	0.0	0.50×10^6

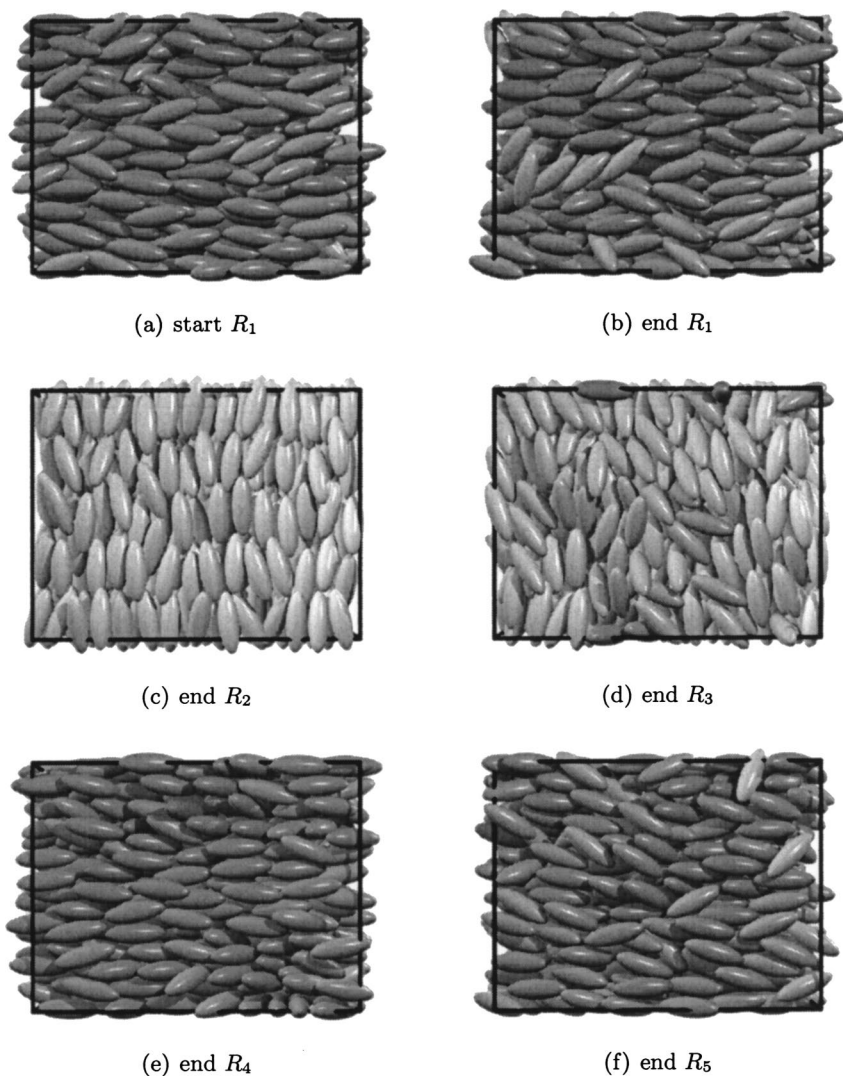


FIG. 13. Configuration snapshots corresponding to the initial (start) and final configurations of runs $R_1 - R_5$ described in Sec. IV.

Configuration snapshots corresponding to the initial and final states from each run in this series are shown in Fig. 13(a)–13(f). The corresponding behaviors of \overline{Q}_{zz}^{Su} and \overline{Q}_{zz}^{Bu} , as a function of the number of MC sweeps, are shown in Fig. 14(a) and 14(b). Also, for comparison, the values of \overline{Q}_{zz} observed in our previous runs at this state point are shown as horizontal lines.

The results confirm that, for the “time scales” accessible to these simulations, the bistability implied by Fig. 11(c) is fully realizable. Run R_1 shows that the initial system remained stable in its planar arrangement; after reorientation of the particles along \hat{z} by the applied field (run R_2), the system equilibrated naturally to a homeotropic arrangement (run R_3) although the final values adopted by \overline{Q}_{zz} proved higher than those obtained from the previous runs performed at this state point. This discrepancy may have been a consequence of the relatively high field strength employed in run R_2 which induced almost perfect homeotropic alignment in the near-substrate region. Thus, while the bulk of the system equilibrated towards the stable homeotropic state upon removal of the field, packing constraints in the surface region may have inhibited particles from adopting planar orientation close to the surface (as was seen for a small number of particles in

the previous simulations). We do not think that this brings into question the equilibration of the state observed here. Reapplication of the field with a negative molecular dielectric anisotropy (run R_4) then generated a strongly planar arrangement which relaxed to the original stable state upon field removal (run R_5). In this case, the system equilibrated to the same values of \overline{Q}_{zz} as those obtained previously. It should be noted also that the “response times” of the systems were different in the bulk and interfacial regions; no precise information can be inferred from this, however, since the true time evolution of the system cannot be determined from our MC simulations.

V. CONCLUSIONS

In this paper we have studied the behavior of liquid-crystalline systems confined in slab geometry between symmetric walls. For the simple HNW potential used here, we have shown that the preferred anchoring direction is controlled by the particle–substrate interaction needle length, k_S . At nematic densities, all of the systems simulated have exhibited a homeotropic to planar anchoring transition on increase in k_S . As well as having orthogonal bulk alignments,

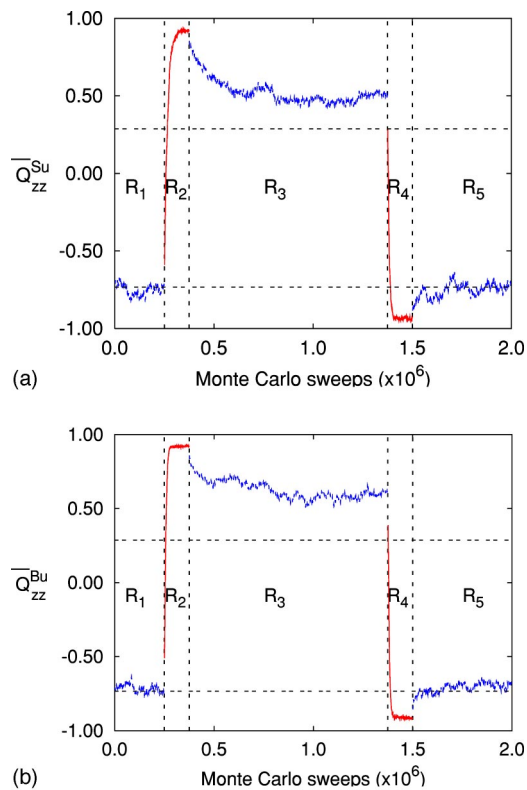


FIG. 14. (Color online) Evolution of \overline{Q}_{zz} in the (a) interfacial and (b) bulk regions as a function of the number of Monte Carlo sweeps.

the homeotropic and planar states have been shown to involve distinct surface arrangements, with little configurational overlap.

The anchoring transition observed here appears to be first order because of both the associated discontinuity in the anchoring orientation and the configurational hysteresis (or bi-

stability) observed. This bistability has been found over a relatively narrow parameter window, but has proved highly reproducible with both states being very long lived. Presumably, this longevity is related to the configurational distinctiveness of the two surface states and the anchoring-orientation-conserving effect of the overlying nematic fluid. It should be possible to characterize this bistability more quantitatively by using reweighting techniques to determine the form of free-energy barrier separating the stable states; the height of this ρ^* -dependent barrier height sets the time scale of any spontaneous switching between the states and, so, knowledge of it would enable some sort of comparison to be made with bistable experimental systems.

Rather surprisingly, the anchoring behavior of this system has shown very little dependence on the system density; the limits of the bistability regions are, essentially, isochores. One consequence of this has been that the approximate transition needle lengths, k_s^T , calculated in the high packing limit, have proved reasonably accurate for all nematic densities. Put another way, this suggests that even at ρ_{NI}^* , this system was aware of the two states' particle-volume absorption efficiencies in the high packing limit. This counterintuitive result is presumably a consequence of the simplicity of the HNW model used here: we will revisit this issue, and the routes it offers for manipulation of the bistability region, in future work employing models with less idealized particle-substrate interactions [52]. Specifically, focus will be brought to bear on the influence of the particle-surface contact function on the surface anchoring behavior and the size and shape of the bistability region.

ACKNOWLEDGMENTS

We wish to acknowledge useful discussions with Dmytro Antipov, Chris Care, and Paulo Teixeira and Sheffield Hallam University's Materials Research Institute for financial support.

-
- [1] B. Jérôme, *Phys. Rep.* **54**, 391 (1991).
 [2] M. Schoen, *Ber. Bunsenges. Phys. Chem.* **100**, 1355 (1996).
 [3] M. Schoen, *J. Chem. Phys.* **105**, 2910 (1996).
 [4] J.S. Patel and H. Yokoyama, *Nature (London)* **362**, 525 (1993).
 [5] P. Jagemalm and L. Komitov, *Liq. Cryst.* **23**, 1 (1997).
 [6] R. Barberi, M. Giocondo, M. Iovane, I. Dozov, and E. Polosat, *Liq. Cryst.* **25**, 23 (1998).
 [7] Y-M. Zhu, Z-H. Lu, X.B. Jia, Q. H. Wei, D. Xiao, Y. Wei, Z. H. Wu, Z. L. Hu, and M. G. Xie, *Phys. Rev. Lett.* **72**, 2573 (1994).
 [8] Y-M. Zhu and Y. Wei, *J. Chem. Phys.* **101**, 10023 (1994).
 [9] G. Barbero and V. Popa-Nita, *Phys. Rev. E* **61**, 6696 (2000).
 [10] B. Alkhairalla, H. Allinson, N. Boden, S. D. Evans, and J. R. Henderson, *Phys. Rev. E* **59**, 3033 (1999).
 [11] B. Alkhairalla, N. Boden, E. Cheadle, S. D. Evans, J. R. Henderson, H. Fukushima, S. Miyashita, H. Schonherr, G. J. Vancso, R. Colorado, M. Graupe, O. E. Shmakova, and T.R. Lee, *Europhys. Lett.* **59**, 410 (2002).
 [12] B. Jerome J. O'Brien, Y. Ouchi, C. Stanners, and Y. R. Shen, *Phys. Rev. Lett.* **71**, 758 (1993).
 [13] D. N. Stonescu, P. Martinot-Lagarde, and I. Dozov, *Mol. Cryst. Liq. Cryst. Sci. Technol., Sect. A* **329**, 339 (1999).
 [14] T. J. Sluckin, *Physica A* **213**, 105 (1995).
 [15] P. I. C. Teixeira and T. J. Sluckin, *J. Chem. Phys.* **97**, 1498 (1992).
 [16] P. I. C. Teixeira and T. J. Sluckin, *J. Chem. Phys.* **97**, 1510 (1992).
 [17] P. I. C. Teixeira, T. J. Sluckin, and D. E. Sullivan, *Liq. Cryst.* **14**, 1243 (1993).
 [18] T. Zheng Qian and P. Sheng, *Phys. Rev. Lett.* **77**, 4564 (1996).
 [19] T. Zheng Qian and P. Sheng, *Phys. Rev. E* **55**, 7111 (1997).
 [20] J. G. Gay and B. J. Berne, *J. Chem. Phys.* **74**, 3316 (1981).
 [21] Z. Zhang, A. Chakrabarti, O. G. Mouristen, and M. J. Zuckermann, *Phys. Rev. E* **53**, 2461 (1996).
 [22] G. D. Wall and D. J. Cleaver, *Phys. Rev. E* **56**, 4306 (1997).

- [23] R. Latham and D. J. Cleaver, *Chem. Phys. Lett.* **330**, 7 (2000).
- [24] G. D. Wall and D. J. Cleaver, *Mol. Phys.* **101**, 1105 (2003).
- [25] T. Gruhn and M. Schoen, *Phys. Rev. E* **55**, 2861 (1997).
- [26] T. Gruhn and M. Schoen, *Thin Solid Films* **330**, 46 (1998).
- [27] T. Gruhn and M. Schoen, *Mol. Phys.* **93**, 681 (1998).
- [28] M. P. Allen, *Mol. Phys.* **96**, 1391 (1999).
- [29] R. van Roij, M. Dijkstra, and R. Evans, *Europhys. Lett.* **49**, 350 (2000).
- [30] R. van Roij, M. Dijkstra, and R. Evans, *J. Chem. Phys.* **117**, 7689 (2000).
- [31] M. Dijkstra, R. van Roij, and R. Evans, *Phys. Rev. E* **63**, 051703 (2001).
- [32] A. Chrzanowska, P. I. C. Teixeira, H. Ehrentraut, and D. J. Cleaver, *J. Phys.: Condens. Matter* **13**, 1 (2001).
- [33] D. J. Cleaver and P. I. C. Teixeira, *Chem. Phys. Lett.* **338**, 1 (2001).
- [34] B. J. Berne and P. Pechukas, *J. Chem. Phys.* **56**, 4213 (1972).
- [35] D. J. Cleaver and D. J. Tildesley, *Mol. Phys.* **81**, 781 (1994).
- [36] M. Yoneya and Y. Iwakabe, *Liq. Cryst.* **18**, 45 (1995).
- [37] D. J. Cleaver, M. J. Callaway, T. Forester, W. Smith, and D. J. Tildesley, *Mol. Phys.* **86**, 613 (1995).
- [38] D. R. Binger and S. Hanna, *Liq. Cryst.* **26**, 1205 (1999).
- [39] D. R. Binger and S. Hanna, *Liq. Cryst.* **27**, 89 (2000).
- [40] D. R. Binger and S. Hanna, *Liq. Cryst.* **28**, 1215 (2001).
- [41] T. P. Doerr and P. L. Taylor, *Mol. Cryst. Liq. Cryst. Sci. Technol., Sect. A* **330**, 1735 (1999).
- [42] T. P. Doerr and P. L. Taylor, *Int. J. Mod. Phys. C* **10**, 415 (1999).
- [43] H. Lange and F. Schmid, *J. Chem. Phys.* **111**, 362 (2002).
- [44] H. Lange and F. Schmid, *Eur. Phys. J. E* **7**, 175 (2002).
- [45] H. Lange and F. Schmid, *Comput. Phys. Commun.* **147**, 276 (2002).
- [46] M. Rigby, *Mol. Phys.* **68**, 687 (1989).
- [47] P. Padilla and E. Velasco, *J. Chem. Phys.* **106**, 10299 (1997).
- [48] E. de Miguel and E. Martín del Río, *J. Chem. Phys.* **115**, 9072 (2001).
- [49] E. de Miguel and E. Martín del Río, *J. Chem. Phys.* **118**, 1852 (2003).
- [50] F. Barmes, Ph.D. thesis, Sheffield Hallam University, 2003.
- [51] P. I. C. Teixeira, F. Barmes, and D. J. Cleaver, *J. Phys.: Condens. Matter* (to be published).
- [52] F. Barmes and D. J. Cleaver (unpublished).
- [53] E. de Miguel, *Phys. Rev. E* **47**, 3334 (1993).
- [54] N. V. Priezjev, G. Skačej, R. A. Pelkovits, and S. Žumer, *Phys. Rev. E* **68**, 041709 (2003).
- [55] P. I. C. Teixeira, F. Barmes, and D. J. Cleaver, *J. Phys.: Condens. Matter* **16**, S1969 (2004).